Short-Range Ordering Alters the Dislocation Nucleation and Propagation in Refractory High-Entropy Alloys

Shuai Chen[1,2], Zachary H. Aitken[2], Subrahmanyam Pattamatta[3], Zhaoxuan Wu[4], Zhi Gen Yu[2], David J. Srolovitz[3,5,*], Peter K. Liaw[6,*], Yong-Wei Zhang[2,*]

[1]*Materials Genome Institute, Shanghai University, Shanghai 200444, China*

[2]*Institute of High Performance Computing (IHPC), Agency for Science, Technology and Research (A*STAR), 1 Fusionopolis Way, #16-16 Connexis, Singapore 138632, Republic of Singapore.*

[3]*Department of Mechanical Engineering, The University of Hong Kong, Hong Kong SAR, China*

[4]*Department of Materials Science and Engineering, City University of Hong Kong, Hong Kong SAR, China*

[5]*International Digital Economy Academy (IDEA), Shenzhen, China*

[6]*Department of Materials Science and Engineering, The University of Tennessee, Knoxville, TN 37996, USA*

[*] Email: srol@hku.hk

[*] Email: pliaw@utk.edu

[*] Email: zhangyw@ihpc.a-star.edu.sg

Abstract

The role of short-range ordering (SRO) in the dislocation kinetics in refractory high-entropy alloys (RHEAs) remains controversial. On one hand, it was shown by simulations that the mobility of edge dislocations was enhanced while that of screw dislocations was reduced, leading to the conclusion that screw dislocations should be dominant. On the other hand, experiments exclusively showed the dominance of edge dislocations. Here, we investigate the impact of SRO in the grain interior and grain boundary on dislocation nucleation and propagation in a BCC MoTaTiWZr RHEA, using a combination of the density-functional theory calculations, Monte Carlo method, and molecular dynamic simulation. Our results show that this RHEA is energetically favorable to undergo SRO, thus forming a pseudo-composite microstructure. This microstructure consists of three categories of clusters: high energy clusters (HECs), medium energy clusters (MECs), and low energy clusters (LECs), with the HECs in grain boundaries acting as weak fillers to induce dislocation nucleation while the MECs/LECs serving as a strong matrix to stabilize the weak HECs. Importantly, SRO is found to enhance the energy barriers for both edge and screw dislocation motion and make the mobility of edge dislocations comparable to or even lower than screw dislocations, contributing to the dominance of edge dislocations in the BCC RHEA. Our work highlights the importance of SRO in influencing the dislocation activity of RHEAs and presents a fascinating route for designing RHEAs to achieve superior mechanical properties.

Key words: Refractory high-entropy alloys, Short-range ordering, Dislocation nucleation, Dislocation propagation

Introduction

Metallic alloys composed of five or more metallic elements with near equi-atomic concentrations are now widely known as compositionally complex[1] or high-entropy alloys[2] (HEAs). They have drawn extensive attention from both the scientific and industrial communities for their exceptional mechanical properties under extreme conditions, which are important for high-performance structural material applications[3,4]. For example, as a new class of structural materials, CoCrNi/CoFeNi/CoCrFe-based (Cantor-like) face-centered-cubic (FCC) HEAs exhibited superior strength and exceptional ductility[5-7]. Another prominent class of HEAs are refractory HEAs (RHEAs), which are composed of refractory elements (Mo, W, Ta, Ti, Zr, Nb, V, etc.) and form a body-centered-cubic (BCC) lattice structure. Refractory HEAs are considered promising candidates for structural materials at elevated temperature due to their extremely high melting temperatures[8-11].

Plastic deformation in metals and alloys are usually carried by dislocations, which commonly govern post-yield mechanical properties[12]. Many studies have demonstrated that RHEA dislocation behavior is highly dependent upon their micro-/nano-structures[13,14]. Understanding the dislocation-structure relations of RHEAs enables rational alloy design. Despite intense research, the fundamental mechanisms behind several remarkable dislocation-related phenomena in BCC RHEAs remain unclear. For example, edge dislocations are normally highly mobile in conventional BCC metals/alloys and rapidly disappear from the material[15]. Yin et al.[16] also found that the mobility of edge dislocations is enhanced by the presence of short-range ordering (SRO) in BCC MoNbTaW RHEAs, whereas the rate of double-kink nucleation in the motion of screw dislocations is reduced using molecular dynamics (MD) simulations. Therefore, the remaining screw dislocations should be the dominant dislocation type in RHEAs.

However, Wang et al. observed the unexpected dominance of non-screw character dislocations in MoNbTi alloys via a scanning electron microscope operating in a transmission mode[17]. Similarly, Lee et al. also found the dominance of edge dislocations in NbTaTiV and CrMoNbV RHEAs via neutron diffraction peak-broadening modeling and analysis and verified through scanning transmission electron microscopy studies[8,9]. Moreover, Li et al. reported the prevalence of edge dislocations in a $Ti_2ZrHfV_{0.5}Ta_{0.2}$ RHEA[10]. The presence of edge dislocations was also observed in the TiZrHfNbTa RHEA by Dirras et al.[11]. This strong contrast between simulation results[16] and experimental observations[8-11,17] provides the motivation for this study.

Solid-solution strengthening has been proposed as a key strengthening mechanism in both FCC and BCC HEAs[18-20]. In contrast to this ideal random solid solution (RSS), experimental results have provided direct evidence for the wide presence of SRO in HEAs[21,22] or medium-entropy alloys[23,24]. It has been widely recognized that multiple levels of heterogeneities, including the atomic-level SRO, play a significant role in controlling the deformation mechanisms and mechanical properties of HEAs[25,26]. Several important questions arise. Are chemical-affinity disparity and exclusivity the driving forces responsible for the SRO in BCC RHEAs[27]? What is the role of SRO in the deformation mechanisms of BCC RHEAs? Is SRO responsible for the dominance of edge dislocations in these RHEAs? Clearly, answers to these interesting questions are critical to guide the design and processing of BCC RHEAs.

Since SRO is an atomic-level phenomenon, it is extremely challenging to experimentally interrogate its formation or evolution. Atomistic simulations are important tools to reveal the fundamental mechanisms behind the observations in the HEAs. Due to the high computational cost, density-functional theory (DFT) calculations of HEAs are limited to special quasi-random

structures (SQS)[28] and a small set of ordered structures (SSOS)[29,30] methods. Monte Carlo (MC) and MD simulations can provide insight into SRO in HEAs on a larger time and size scale[16,26,27,31]. For example, Li et al.[31] studied SRO and strengthening in single-crystal and polycrystalline NbMoTaW RHEAs through hybrid MC/MD simulations. In the single-crystal RHEA, simulations[31] showed a greatly-reduced anisotropy in the critically resolved shear stress between edge and screw dislocations, as compared with the elemental metals. In the polycrystalline RHEAs, thermodynamically-driven Nb segregation to the grain boundaries (GBs) and W enrichment within the grain interiors (GIs) were observed. The increased GB stability associated with Nb enrichment reduces the von Mises strain, leading to a higher strength than the RSS counterparts.

Here, we perform hybrid DFT/MC/MD simulations to explore the impacts of SRO within GIs and GBs on the dislocation activity in an equiatomic BCC MoTaTiWZr RHEA. Density-functional theory calculations are applied to verify the accuracy of interatomic potentials in the MC/MD simulations, MC is employed to exchange atoms of different types to lower the alloy energy by optimizing SRO, and MD is used to both relax the local atomic structure/displacements and to simulate tensile deformation. The Warren-Cowley parameters[32] (WCPs) for all elemental 1st nearest neighbor pairs describe SRO. Our MC/MD simulations, using DFT-validated interatomic potentials, show that SRO development in the MoTaTiWZr RHEA is energetically favored. This SRO produces a pseudo-composite microstructure consisted of three types of clusters: high energy clusters (HECs), medium energy clusters (MECs), and low energy clusters (LECs), with the HECs in GBs acting as weak fillers to induce dislocation nucleation and the MECs/LECs serving as a strong matrix to stabilize the weak HECs. Short-range ordering also increases the energy barriers

for both edge and screw dislocation motions and makes the mobility of edge dislocations comparable to or even lower than screw dislocations, resulting in the unique dominance of edge dislocations in BCC RHEAs. These new discoveries of SRO behaviors in the RHEAs will facilitate the development of refractory alloy systems for structural material applications.

Results

Short-range ordering in grain interiors and grain boundaries. The MoTaTiWZr RHEA simulation model is constructed by aligning two crystallographically equivalent grains (G1 and G2) in different orientations ($[11\bar{2}]_{G1}$ and $[1\bar{1}0]_{G2}$) to form a pair of grain boundaries, GB1 and GB2, as shown in Fig. 1a. Hybrid MC swaps and MD relaxations (run iteratively) are performed in both grains simultaneously at 300 K to obtain energetically-favourable atomic configurations. The variation of the potential energy per atom for the MoTaTiWZr RHEA with iterations is shown as the red curve in Fig. 1b (PE1). The potential energy per atom at 0, 0.5×10^6 (0.5M), and 1×10^6 (1M) iterations is -7.008, -7.083, and -7.092 eV/atom, respectively. Furthermore, a certain number of iterations are performed in the 1-nm-thick regions with GBs according to the ratio of its atom quantity to the whole box and the number of iterations performed in the grains. The evolution of the potential energy per atom for the RHEA as a function of iterations is shown as a black curve in Fig. 1b, i.e., 0.05×10^6 iterations for the 0.5M sample (PE2) and 0.1×10^6 iterations for the 1M sample (PE3). The potential energy per atom of the 0.5M sample is further reduced from -7.083 to -7.085 eV/atom, and that of the 1M sample is decreased from -7.092 to -7.094 eV/atom.

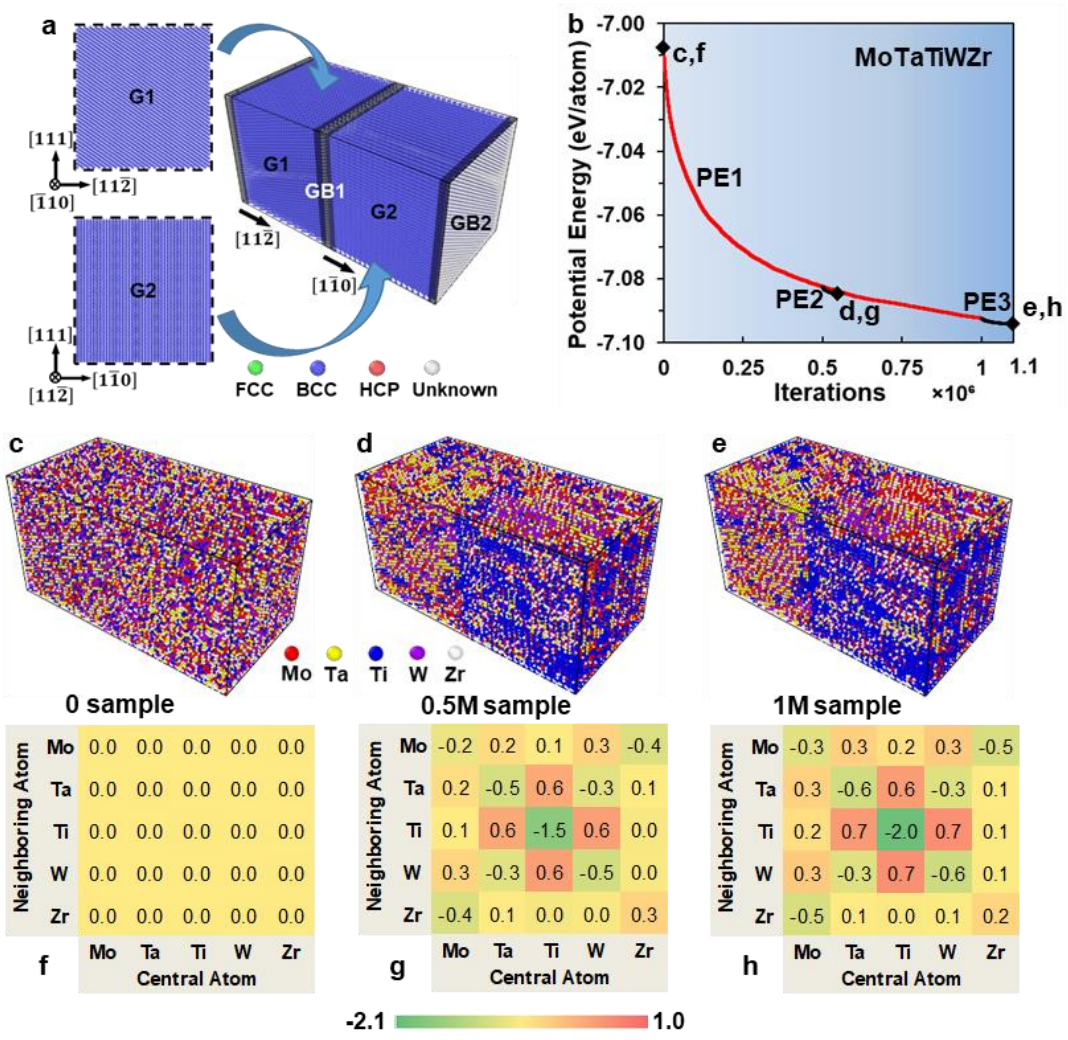

Fig. 1 Simulation model, potential energy, atomic configurations, and Warren-Cowley parameters of the MoTaTiWZr RHEA during iterations at 300 K. a Periodic bicrystal model of two different orientated grains (G1 and G2) meeting at a pair of grain boundaries (GB1 and GB2). **b** Variation of the total potential energy with iterations. Atomic configurations are colored according to atom types and tables of Warren-Cowley parameters at 0 (**c** and **f**), 0.5M (**d** and **g**), and 1M (**e** and **h**) iterations, as indicated in **b**.

The atomic configurations and corresponding WCPs of G1 are presented in Figs. 1c-e (atoms colored according to the elemental type) and Figs. 1f-h (negative values of the WCP indicate favourable atomic pairs, i.e., SRO) at different steps. Figures 1c and 1f indicate that the initial

configuration (the 0 sample) is an RSS, and all WCPs are zero (no SRO). Figures 1d/e and g/h demonstrate that there is a strong tendency to form Ti-Ti pairs (WCP = -1.5/-2.0) and, to a lesser extent, W-W (WCP = -0.5/-0.6), Ta-Ta (WCP = -0.5/-0.6), and Mo-Zr (WCP = -0.4/-0.5) pairs. There is also a weak tendency to form Ta-W (WCP = -0.3), and Mo-Mo (WCP = -0.2/-0.3) pairs. The WCPs of G2 for the 0, 0.5M, and 1M samples are shown in the Supplementary Tables 1a-c, demonstrating good consistency with those in Figs. 1f-h due to the crystallographic equivalency of G1 and G2. However, there exist minor differences in their WCPs due to the different random numbers used during MC swaps.

To understand the observed SRO in the GIs, we examine the cohesive energies for 10 binary combinations of {Mo, Ta, Ti, W, and Zr} in the AB B2 intermetallic crystal structure and 5 single elements of {Mo, Ta, Ti, W, and Zr} in the BCC crystal structure. The cohesive energies determined from the interatomic potentials used in the MD and from DFT are listed in the Supplementary Tables 2a and 2b. While the MD interatomic potential-based cohesive energies do not demonstrate perfect agreement with DFT calculations (as expected), they are remarkably successful in reproducing the important trends. For example, both results indicate that Ti-Ti exhibits the highest cohesive energy, Mo-Zr and Mo-Mo are of medium cohesive energies, and Ta-W, Ta-Ta, and W-W have lower cohesive energies. Besides, we also check the stacking fault energy (SFE) and surface energy (SE) (Supplementary Fig. 1). The calculated SFE and SE values of MoTaTiWZr using MD interatomic potential are 0.8 J/m^2 and 1.7 J/m^2, respectively. These values are consistent with the SFE (0.4 - 1.2 J/m^2) and SE (1.5 - 2.5 J/m^2) of most binary, ternary, and quaternary alloys consisting of {Mo, Ta, Ti, W, Zr, Hf, V, Nb} in literature[33]. Using the absolute values of cohesive energies in the Supplementary Table 2a, we calculate the chemical

affinity (CA, the definition is given in Method section) of atomic pairs in terms of the normalized cohesive energy (Supplementary Table 2c, the high/low cohesive energy implies weak/strong CA).

In general, we are able to divide the constituent elemental pairs (in Supplementary Table 2c) into three classes according to CA, that is, a low-energy cluster (LEC) with strong CA ($0.75 < CA_{ij} \leq 1.0$), a medium-energy cluster (MEC) with medium CA ($0.35 \leq CA_{ij} \leq 0.75$), and a high-energy cluster (HEC) with weak CA ($0 \leq CA_{ij} < 0.35$). CA_{WW} (= 1.0), CA_{TaW} (= 0.9), and CA_{TaTa} (= 0.8) are quite high and have large disparity with other values in the Supplementary Table 2c, leading to the formation of LECs between W and Ta (WCP_{WW} = -0.6, WCP_{TaW} = -0.3, and WCP_{TaTa} = -0.6 in Fig. 1h). Besides W and Ta atoms, CA_{MoZr} (= 0.5) and CA_{MoMo} (= 0.5) are higher than CA of other pairs among Mo, Zr, and Ti atoms. The negative values of WCPs in Fig. 1h, i.e., WCP_{MoZr} (= -0.5) and WCP_{MoMo} (= -0.3) verify the formation of these MECs. The LECs and MECs (with a preponderance of W-W, Ta-W, Ta-Ta, Mo-Zr, and Mo-Mo pairs) do not include Ti atoms (*i.e.*, chemical-element exclusivity). Consequently, Ti atoms bond with neighboring Ti atoms (WCP_{TiTi} = -2.0 in Fig. 1h) despite the formation of HECs. These trends clearly demonstrate that the chemical-affinity disparity and chemical-element exclusivity[27] drive the SRO in the GIs of MoTaTiWZr RHEAs.

To analyse the SRO in GBs (GB1 and GB2) of MoTaTiWZr RHEAs, we calculate the variation in the numbers of neighbouring pairs as a function of separation distance (Fig. 2a). The unrecognized structures according to common neighbour analysis (CNA)[34] are identified as GBs (i.e., central atoms in Figs. 2b-g). The results indicate that the 1st-nearest neighbor distances in GB1 and GB2 range from 2.5 to 3.75 Å (atomic pairs in this range are defined as 1st nearest neighbors for the calculation of the WCP). The WCPs of GB1 and GB2 are shown in Figs. 2b-d

and Figs. 2e-g, respectively. Comparisons of the GB1 and GB2 WCPs demonstrate that the two GBs are structurally similar, albeit with minor differences. For example, WCPs of Ti-neighboring pairs (Mo-Ti, Ta-Ti, Ti-Ti, W-Ti, and Zr-Ti) are remarkably similar in both GBs. However, the WCPs for Zr-neighboring pairs (Mo-Zr, Ta-Zr, and W-Zr) are of large magnitude only in GB1, while those for Mo-neighboring pairs (Mo-Mo, Ta-Mo, W-Mo, and Zr-Mo) are large only in GB2. Therefore, HECs (Ti-neighboring pairs) and MECs (Mo- and Zr-neighboring pairs) are predominantly formed in GBs. We also investigated the effect of annealing temperature on SRO in GIs and GBs of MoTaTiWZr RHEAs (Supplementary Fig. 2, Supplementary Table 3 and Supplementary Results: Effect of annealing temperature on SRO of MoTaTiWZr RHEAs), and the effect of grain orientation and GB topology on SRO in GIs and GBs of MoTaTiWZr RHEAs (Supplementary Figs. 3 and 4, and Supplementary Results: Effect of grain orientation and GB topology on SRO of MoTaTiWZr RHEAs).

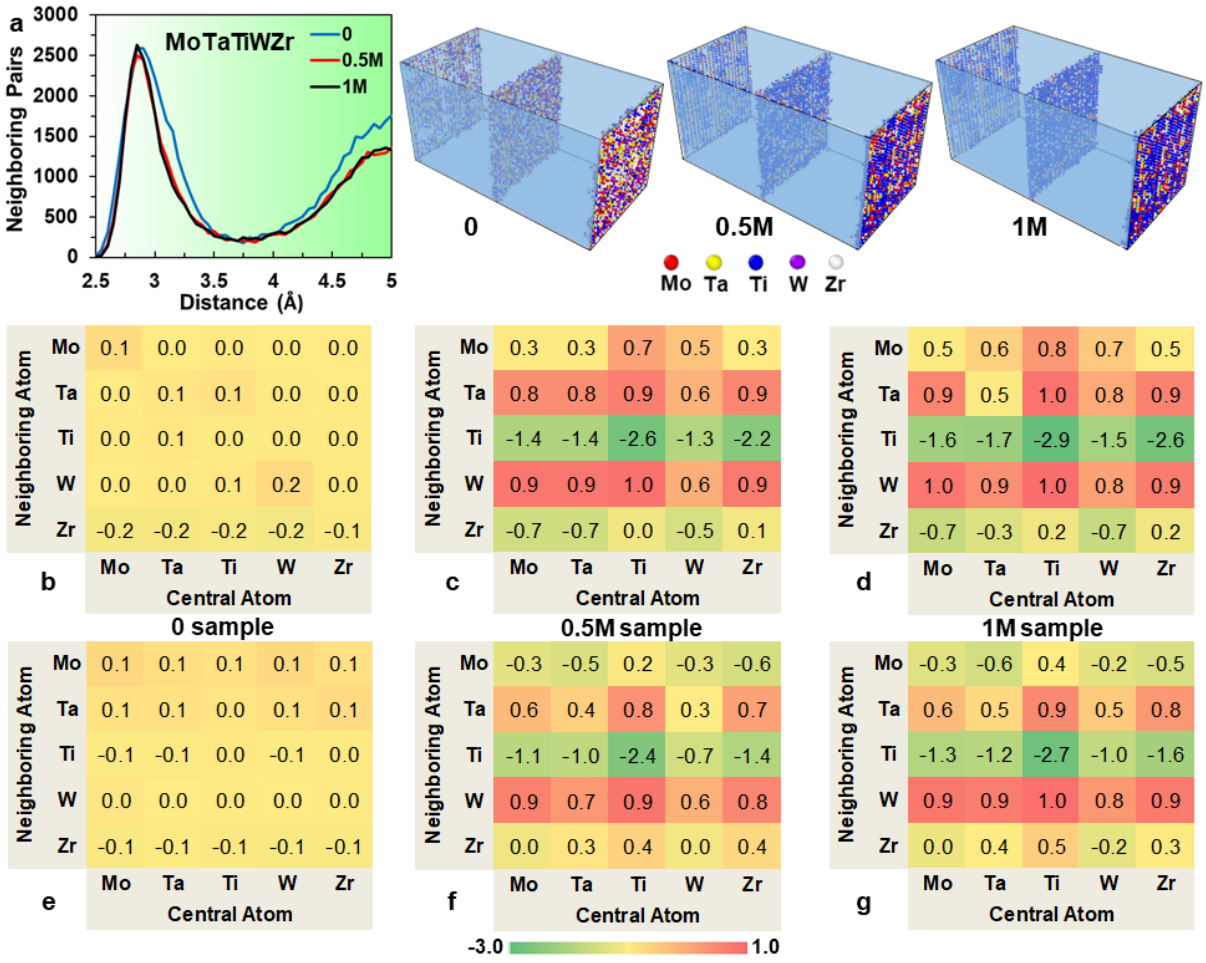

Fig. 2 Number of neighboring pairs, atomic configurations, and Warren-Cowley parameters of grain boundaries. a Variation of numbers of neighboring pairs with separation distance and grain-boundary configurations of 0, 0.5M, and 1M samples. Warren-Cowley parameters of grain boundaries **b** GB1 and **e** GB2 in the 0 sample, **c** GB1 and **f** GB2 in the 0.5M sample, and **d** GB1 and **g** GB2 in the 1M sample.

Impact of GB short-range ordering on dislocation nucleation. To investigate the effect of SRO on dislocation activities in the MoTaTiWZr RHEA, uniaxial tensile deformation simulations were performed on the 0, 0.5M, and 1M samples (strain rate of 1×10^8 s^{-1} at 300 K and 1,200 K). The corresponding uniaxial stress-strain curves are plotted in Fig. 3a. Figures 3b-f present the dislocation structures of the 0-300K, 0.5M-300K, and 1M-300K samples according to dislocation

analysis (DXA)[35] prior to (Figs. 3b and 3c) and at the peak stress (Figs. 3d-f). There is no dislocation generation prior to the peak stress. Dislocations were generated at the GBs at the peak stress, suggesting that dislocation nucleation dominates the peak stress at 300 K. The Supplementary Fig. 5 presents the dislocation structures tested at 1,200 K, indicating that the dominant mechanism remains dislocation nucleation at high temperature. All nucleated dislocations in Fig. 3 and Supplementary Fig. 5 have a Burgers vector of 1/2 ⟨111⟩, which represents a full dislocation. The {112} (Schmid factor: 0.314) and {123} (Schmid factor: 0.309) slip systems are activated, where the full dislocations lie on.

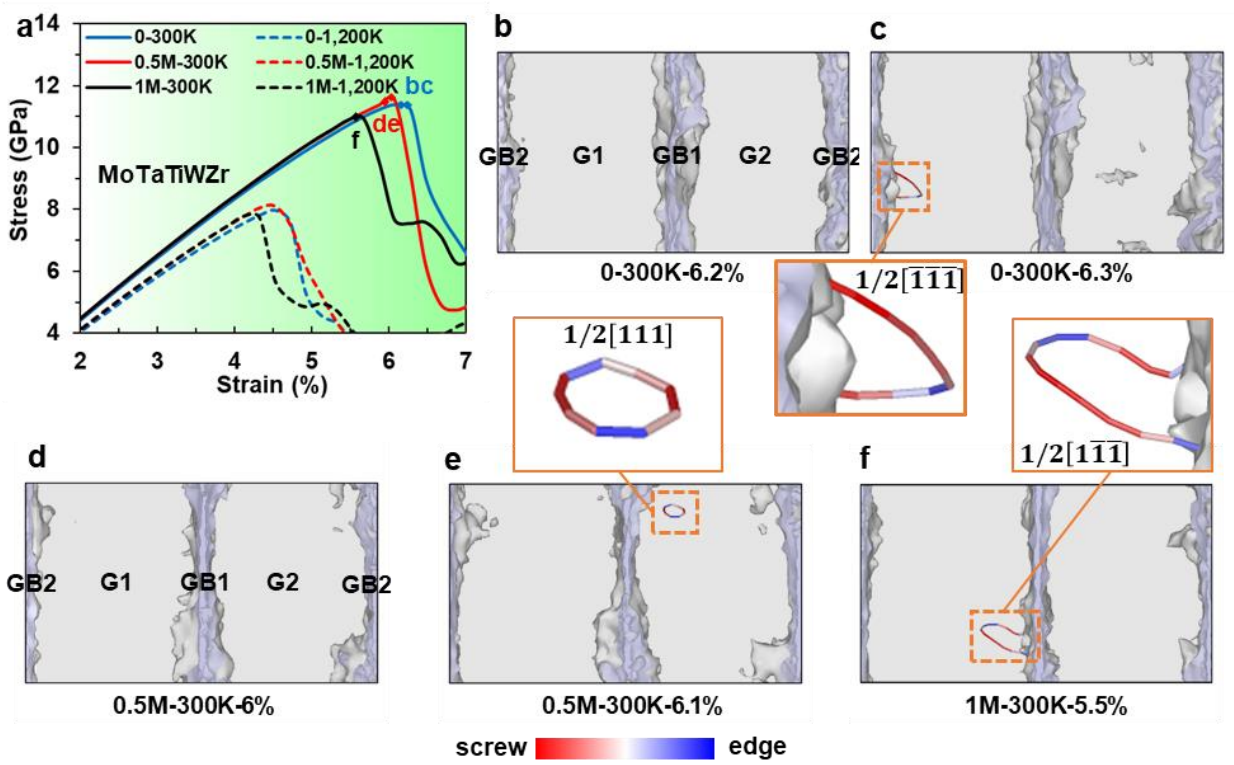

Fig. 3 Stress-strain curves and dislocation structures of the MoTaTiWZr RHEA. a Variation of stress with strain for the samples after 0, 0.5 × 10^6 (0.5M), and 1 × 10^6 (1M**)** iterations at 300 K during tension at 300 K (0-300K, 0.5M-300K, and 1M-300K) and 1,200 K (0-1,200K, 0.5M-1,200K, and 1M-1,200K). Dislocation structures under tension at 300 K prior to the peak stress: **b** 0-300K sample at a 6.2% strain,

and **c** 0-300K sample at a 6.3% strain, and at the peak stress: **d** 0.5M-300K sample at 6% strain, **e** 0.5M-300K sample at a 6.1% strain, and **f** 1M-300K sample at a 5.5% strain, as indicated in **a**.

It is noted that there is a dislocation loop nucleated in the 0.5M-300K sample (Fig. 3e). To reveal the origin of dislocation-loop nucleation, we analyze the atomic structures and elemental concentrations at the nucleation site (Supplementary Fig. 6). Atomic structures in some local regions near GBs are distorted during tension (Supplementary Fig. 6b) and grow larger as deformation proceeds (Supplementary Fig. 6c). When the distorted structure is sufficiently large, a dislocation loop will homogeneously nucleate to lower its energy (Supplementary Fig. 6d). Further tension will facilitate the expansion of dislocation loop (Supplementary Fig. 6e). The nucleation site is a distorted BCC structure with Ti-rich HECs, where a 1/2 $[\bar{1}\bar{1}\bar{1}]$ dislocation loop nucleates in the {123} slip plane (Supplementary Fig. 6f). We also explored the effect of annealing temperature on dislocation activities of MoTaTiWZr RHEAs (Supplementary Fig. 7, and Supplementary Results: Effect of annealing temperature on dislocation activities of MoTaTiWZr RHEAs).

To study the effect of SRO on dislocation nucleation, we examine the distribution of three different energy clusters according to their local atomic environment. If the Ti concentration is larger than the concentration of any other four element within the second nearest neighbour of one atom, the atom has a Ti-rich environment and thus belongs to HEC. If the Ti concentration is not the highest, and the concentrations of Ta and W are higher than those of Mo, Ti and Zr, the atom belongs to LEC. Otherwise, it belongs to MEC. Atomic fractions of different energy clusters (HECs, MECs, and LECs) as a function of distance from the dislocation-nucleation site for the 0-300K, 0.5M-300K, and 1M-300K samples are shown in Figs. 4a-c, respectively. The

corresponding atomic configurations for different energy clusters are shown in Figs. 4d-f, respectively, where the dotted circles mark dislocation-nucleation sites. Clearly, dislocation nucleation location is highly correlated with Ti-rich HECs in the 0.5M-300K and 1M-300K samples as these HECs are less stable (easier to generate dislocations) than MECs and LECs during tensile deformation.

A dislocation is nucleated from a Ti-rich zone in the GB due to its high energy state and lattice distortions (Figs. 3b-c and Supplementary Figs. 8a-b). Accompanying the nucleation and subsequent propagation, there is a stress relaxation, which causes the reduction in the stress from the peak stress (Supplementary Figs. 8b-d). Atomic fractions in the dislocation-nucleation and dislocation-propagation region, atomic configurations of different energy clusters, and dislocation structures for the samples after 0.5×10^6, and 1×10^6 iterations at 1,500 K under tension at 300 K are shown in the Supplementary Fig. 9. The results for high-temperature iterated samples also demonstrate that dislocation nucleation is highly dependent on Ti-rich HECs in SRO samples. BCC Ti is dynamically unstable at low temperatures[36], while it could be stabilized by Mo[37], Ta[38,39] and W[40] according to their phase diagram. It is also noted that the HECs are surrounded by LECs/MECs in the SRO sample. Hence, the MECs/LECs serve as a strong matrix to stabilize the weak HECs. We have also explored the effect of SRO on dislocation nucleation in MoTaTiW and MoTaTi alloys, demonstrating similar trends as those observed in MoTaTiWZr RHEAs, i.e., dislocation nucleation dominates the peak stress and nucleation location is highly correlated with HECs (Supplementary Figs. 10-12 and Supplementary Results: SRO and dislocation nucleation in MoTaTiW and MoTaTi alloys). Besides, we have also examined the effect of grain orientation and GB topology on dislocation nucleation (Supplementary Figs. 13-14 and Supplementary

Results: Effect of grain orientation and GB topology on dislocation nucleation). The results also demonstrate that dislocation nucleation dominates the peak stress and the nucleation location is highly correlated with Ti-rich HECs, which is consistent with that in the 0.5M-300K and 1M-300K samples.

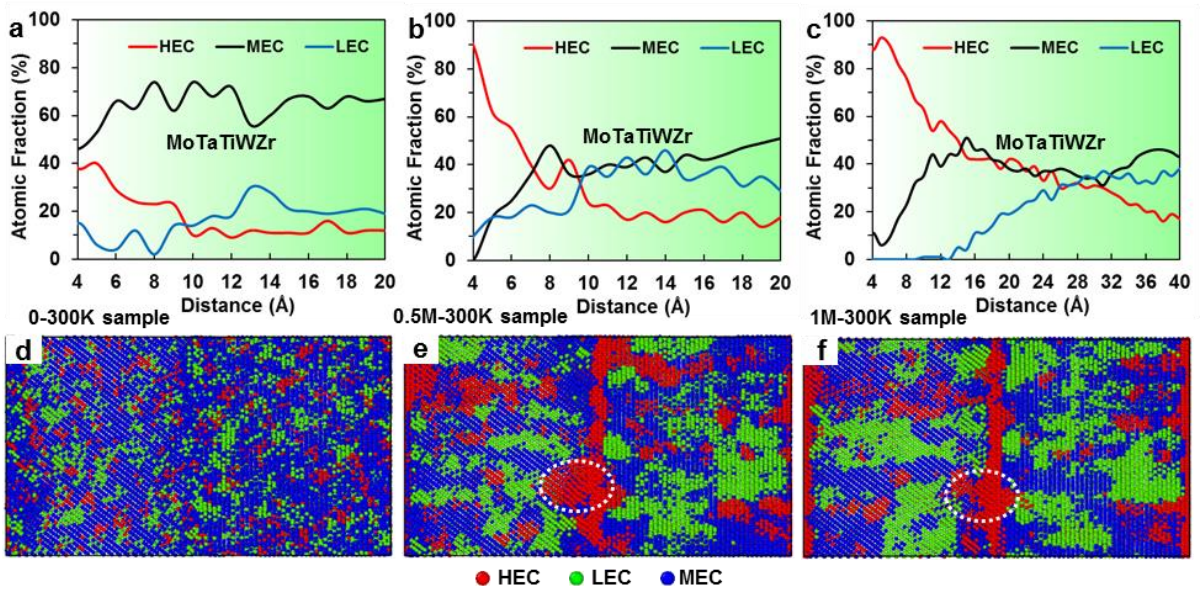

Fig. 4 Atomic fractions of different energy clusters as a function of distance from the dislocation-nucleation site and atomic configurations of different energy clusters in the MoTaTiWZr RHEA. Atomic fractions of different energy clusters (HEC, LEC, and MEC) as a function of distance from the dislocation-nucleation site in **a** the 0-300K sample, **b** the 0.5M-300K sample, and **c** the 1M-300K sample. Atomic configurations of different energy clusters for **d** the 0-300K sample, **e** the 0.5M-300K sample, and **f** the 1M-300K sample. White dotted circles mark the dislocation-nucleation site.

Impact of short-range ordering on dislocation propagation. To quantify the impact of SRO on dislocation activity, we monitored the variations of stress and dislocation character with strain for the 0-300K, 0.5M-300K, and 1M-300K samples (Figs. 5a-c). The density ratio of dislocation character (%) is calculated as the ratio of edge-/screw-dislocation length to the total dislocation

length, where the rest is mixed dislocation. Dislocation structures at strains beyond the peak stress are also shown in Figs. 5d-f. Besides the {112} and {123} slip systems, the {110} slip system (Schmid factor: 0.272) is also activated (i.e., the slip plane of the 1/2 $[\bar{1}11]$ dislocation in the inset of Figure 5f).

Figures 5a and 5d indicate that only edge dislocations are formed at the peak stress in the 0 sample, while screw dislocations are dominate posterior to the peak stress. These trends are consistent with the observations in conventional BCC metals/alloys, where edge dislocations tend to be highly mobile, rapidly gliding out of the system and leaving behind a high density of the slower screw dislocations[15]. It is noted that the density ratios of edge (36%) and screw dislocations (41%) are comparable in the 0.5M-300K sample from 6.6% to 6.8% strain (Figs. 5b and 5e), and edge dislocations predominate (61%) in the 1M-300K sample at 6% strain. We have also examined the density ratios of edge and screw dislocations in MoTaTiW and MoTaTi alloys, which clearly exhibit the similar trends as observed in MoTaTiWZr RHEAs, i.e., edge dislocations play a comparable (or even dominant) role as compared with screw dislocations in the SRO samples post-yield (Supplementary Fig. 15 and Supplementary Results: Density ratios of edge and screw dislocations in MoTaTiW and MoTaTi alloys). These trends are consistent with the experimental observations in MoNbTi[17], NbTaTiV[8], CrMoNbV[9], $Ti_2ZrHfV_{0.5}Ta_{0.2}$[10], and TiZrHfNbTa[11].

We also studied the effect of grain orientation and GB topology on the density ratios of edge and screw dislocations (Supplementary Fig. 16 and Supplementary Results: Density ratios of edge and screw dislocations in MoTaTiWZr with different grain orientations and GB topologies). The results demonstrate that edge dislocations play a comparable (or even dominant) role as compared with screw dislocations in the SRO samples with different grain orientations and GB topologies

post-yield, which is consistent with the trend observed in the 0.5M-300K sample. We also investigated the density ratios of edge and screw dislocations in the 0.5M-1,200K sample (Supplementary Fig. 17). The results indicate that the density ratio of edge dislocations becomes greater (65%) and the strain interval during which the edge dislocations are dominant is also longer (4.8% - 5.4%) at 1,200K. This trend is consistent with the experimental observations of CrMoNbV[9] at 293K and 1,173K.

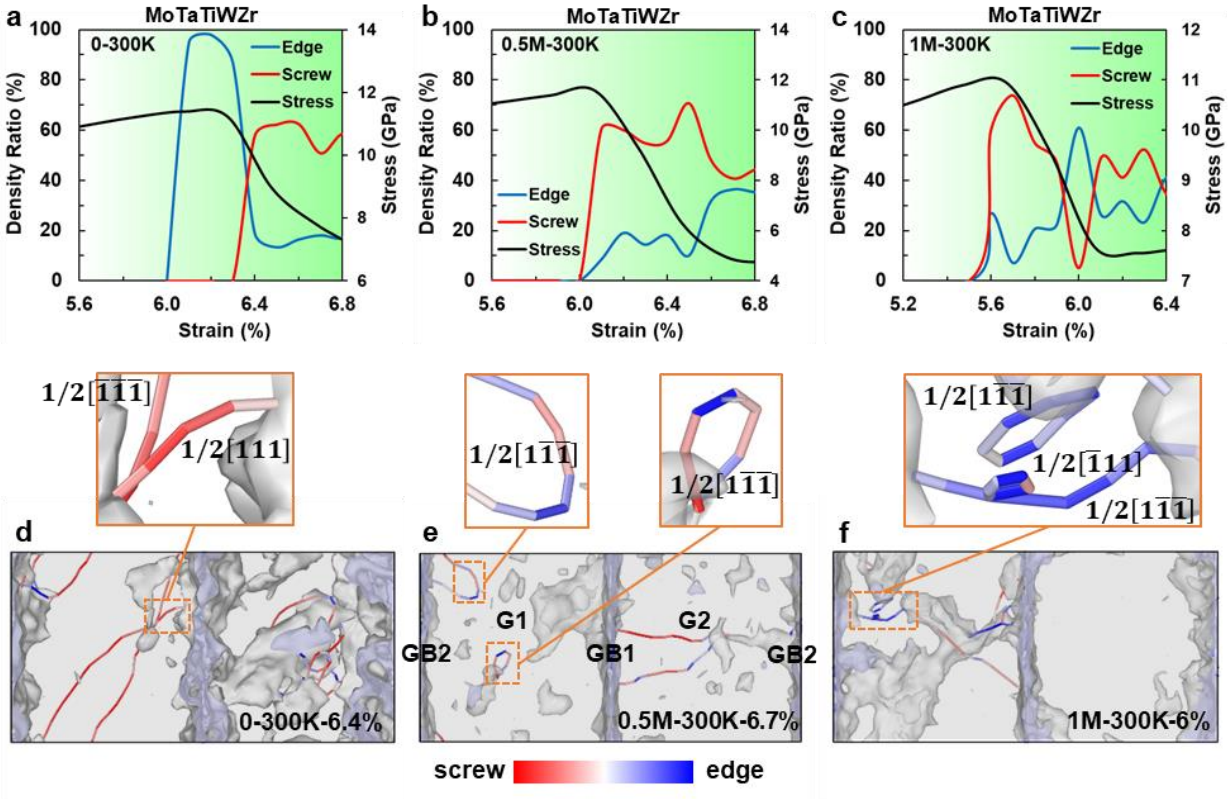

Fig. 5 Stress/dislocation density ratio as a function of strain and dislocation structures of the MoTaTiWZr RHEA. Variation of stress/dislocation density ratio with strain for **a** the 0-300K sample, **b** the 0.5M-300K sample, and **c** the 1M-300K sample, where blue and red curves represent edge and screw dislocations, respectively, and the rest is mixed dislocation. Dislocation structure posterior to the peak

stress: **d** the 0-300K sample at 6.4% strain, **e** the 0.5M-300K sample at 6.7% strain, and **f** the 1M-300K sample at 6% strain.

To reveal the origin of the increased prominence of edge dislocations comparable to screw dislocations in the SRO samples, we calculated the energy landscape sampled by the gliding edge and screw dislocations in SRO and RSS systems using the climbing image nudged elastic band (CINEB)[41] (Fig. 6). The WCPs corresponding to the SRO samples used to generate the edge and screw sample configuration (Supplementary Tables 4a and 4b) show that the degrees of SRO in both the edge- and screw-dislocation models are equal: this is consistent with those in the 0.5M-300K and 1M-300K samples (Figs. 1g and 1h). Comparisons of the red curves between Figs. 6a (Edge-RSS, the dotted box and arrows in Figs. 6c-e marked the moved atoms and their moving direction) and 6b (Screw-RSS, the dotted box and arrows in Figs. 6i-k marked the moved atoms and their moving direction) demonstrate that the energy barrier for core configuration change of edge dislocation during motion (~ 0.1 eV) is much smaller than that of screw (~ 0.3 eV). This is why screws are so much less mobile than edges and are dominant in the 0 sample (Figs. 5a and 5d).

The blue curve in Fig. 6a (Edge-SRO, the dotted box and arrows in Figs. 6f-h marked the moved atoms and their moving direction) indicates that the energy barrier for core configuration change of edge dislocation during motion has a first maximum near 0.5 eV, while that for the screw has a maximum near 0.6 eV (the blue curve in Fig. 6b, Screw-SRO; the dotted box and arrows in Figs. 6l-n marked the moved atoms and their moving direction). Therefore, SRO enhances the energy barriers for both edge and screw dislocation motions. This makes the mobility of edge dislocations comparable to or even lower than that of screw dislocations. This is the origin of the increased

presence of edge dislocations (relative to screw dislocations) seen in the 0.5M-300K (Figs. 5b and 5e) and 1M-300K (Figs. 5c and 5f) samples. The energy curves and energy barriers (0.1 ~ 0.6 eV) are similar to those of CoFeNiTi HEAs reported in the literature (0.2 ~ 0.5 eV)[13], thus providing support for our CINEB calculations.

We calculated the root-mean-squared (RMS) roughness of the dislocation line to evaluate the effect of SRO on the dislocation morphology. The RMS roughness in Edge-RSS is 3.9 Å, while that in Edge-SRO is 5.9 Å. The RMS roughness in Screw-RSS is 2.0 Å, while that in Screw-SRO is 2.1 Å. Therefore, SRO also enhances the roughness of both edge and screw dislocations. However, the impact of SRO on the edge-dislocation roughness (51% increase) is much greater than that for the screw (roughness increases by 5%). We have further explored the interactions between SRO and dislocations, which are consistent with our observations on the mobility of edge and screw dislocations. (Supplementary Fig. 18 and Supplementary Results: Interactions between dislocations and SROs).

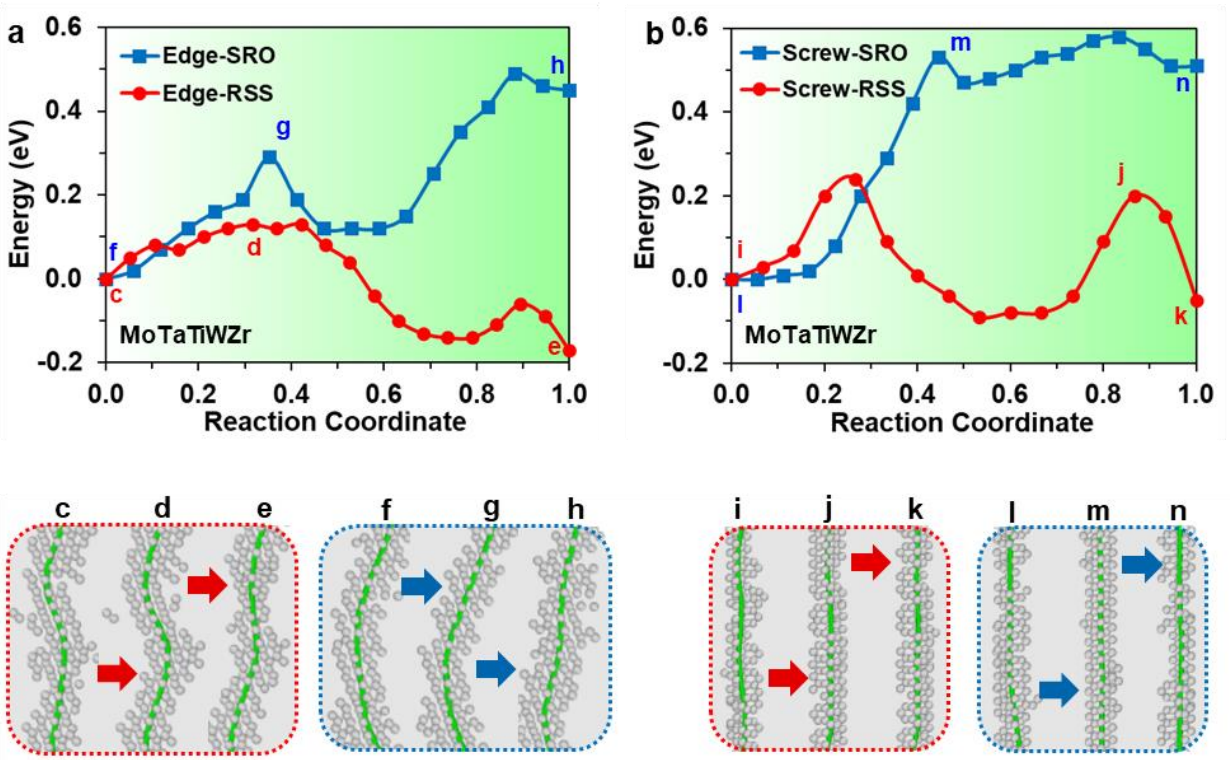

Fig. 6 Minimum energy pathways for the core configuration change of an edge/screw dislocation during motion in the MoTaTiWZr RHEA. The energy landscape sampled during motion of **a** edge and **b** screw dislocation in the RSS and SRO MoTaTiWZr. The moved atoms and their moving direction of edge dislocation in **c-e** the RSS and **f-h** the SRO MoTaTiWZr, as indicated in **a**. The moved atoms and their moving direction of screw dislocation in **i-k** the RSS and **l-n** the SRO MoTaTiWZr, as indicated in **b**.

Discussions

Similarity and difference in SRO between GI and GB. The WCPs of G1 and G2 are largely consistent (compare Fig. 1g/1h with the Supplementary Tables 1b/1c), indicating that the SRO is nearly identical in the different MoTaTiWZr RHEA GIs. There are minor differences in the WCPs of GB1 and GB2 (compare Figs. 2c/2d with Figs. 2f/2g) even though GB1 and GB2 have the same grain-boundary angle (90°). Similar trends have also been observed in FeMnNiCoCr HEA experiments after an aging heat treatment[42]. Li et al. observed that Ni and Mn co-segregate to some

regions of the GBs, while Cr is enriched in other regions of the same GBs where Ni and Mn are depleted[42]. This diversity may be attributed to the flexibility for the formation of local atomic configurations in GBs. This suggests that there is a large design space for SRO in GBs of RHEAs, implying that there is a significant opportunity to tune RHEA GB properties.

In GBs, Ti-neighboring pairs (HECs) and Mo-/Zr-neighboring pairs (MECs) are formed (similar to GIs), while LECs are absent. These trends indicate that the SRO in GBs differ from those in GIs. Similar trends have also been observed in Li et al.'s simulations[30]. Li et al. found remarkable Nb segregation in GBs and W enrichment within GIs of polycrystalline NbMoTaW alloys[30]. They reported that W has the highest strength among the constituent components in pure form, followed by Mo, and Ta and Nb being much weaker. Therefore, Nb is the weakest element in NbMoTaW and likely to segregate into GBs, while W is the strongest element in NbMoTaW and like to stay in GIs. Our results show that Ti-rich HECs are weak and favorable to segregate into GBs, while TaW-rich LECs are strong and prefer to stay in GIs. These trends (weak HECs in GBs and strong LECs in GIs) are consistent with Li et al.'s work (weak Nb in GBs and strong W in GIs)[30].

Comparisons with experiments concerning the effect of SRO on dislocation activity. High-energy clusters are formed along with MECs and LECs via SRO. These HECs in GBs serve as dislocation nuclei, while MECs/LECs play the role of matrix and are not preferential dislocation nucleation sites. The resistance of MECs and LECs to dislocation nucleation may enhance the strength in the MoTaTiWZr RHEA. Increasing SRO leads to increased resistance to dislocation motion and a strength enhancement have also been observed experimentally[22]. The experiments

of Ding et al.[22] showed that increasing SRO in CoCrFeNiPd HEAs led to higher yield strengths, relative to CoCrFeNiMn HEAs.

Without SRO, the difference in the energy barrier between screw dislocation and edge dislocation is large (~0.3 eV vs. ~0.1 eV). SRO clearly increases the energy barrier for both screw and edge dislocations during motion (~0.6 eV vs ~0.5 eV). However, the SRO increases the energy barrier for edge dislocation more than that for screw dislocation, hence making their mobilities comparable. This is consistent with recent experiments[8-11,17]. For example, Wang et al.[17] observed the predominance of non-screw dislocations in MoNbTi alloys. Lee et al.[8,9] found that edge dislocations were more common in NbTaTiV and CrMoNbV alloys. Li et al.[10] reported the prevalence of edge dislocations in a $Ti_2ZrHfV_{0.5}Ta_{0.2}$ RHEA. The presence of edge dislocations was also observed in the TiZrHfNbTa RHEA by Dirras et al.[11]. The alloys reported in the literature, which have observed edge-dislocation dominant/comparable deformation in experiment, are MoNbTi[17], NbTaTiV[8], CrMoNbV[9], $Ti_2ZrHfV_{0.5}Ta_{0.2}$[10], and TiZrHfNbTa[11]. These studies indicate that the edge-dislocation dominant/comparable deformation appears to be universal in BCC refractory medium-/high-entropy alloys. Because the interatomic potentials for these experimental alloy systems are not available in the literature, we have chosen the model RHEA (MoTaTiWZr) for which a reliable interatomic potential is available.

Our findings explain why experimental observations suggest that edge dislocations play a comparable role to screw dislocations in determining the strength of BCC RHEAs[9]. The mechanism behind the edge-dislocation dominant or comparable deformation in RHEAs can be attributed to the enhancement in energy barriers of edge-/screw-dislocation motion by SRO. Besides, through such a comprehensive and detailed simulation study, we can provide plausible

and directly applicable guidelines for future experimental studies on MoTaTiWZr and other RHEAs.

Strategy for exploiting SRO in RHEA design. The tensile deformation simulations described above for RHEAs with different degrees of SRO suggest the importance of SRO. Optimizing the microstructure requires manipulation of the HECs. Conventional HEA strengthening strategies typically focus on forming stable SRO and/or nanoscale precipitates[43], i.e., LECs of the same phase as the matrix produce a small lattice mismatch. Stable SRO and nanoscale precipitates do not cause large stress concentration but do hinder slip. Ding et al.[22] synthesized FCC CoCrFeNiPd and CoCrFeNiMn HEAs and found that CoCrFeNiPd formed more elemental aggregation in small clusters (1-3 nm) than in CoCrFeNiMn and that this led to increased dislocation glide resistance and yield strength without compromising strain hardening or tensile ductility.

In a BCC $Ti_{38}V_{15}Nb_{23}Hf_{24}$ RHEA with secondary nanoscale precipitates (body-centred-tetragonal), Wei et al.[44] found that, if the first dislocation penetrates the nanoscale precipitates, it makes this local structure thermodynamically less favourable, making the precipitate easier for subsequent dislocation penetration (i.e., glide plane softening). Here, we suggest that rather than simply designing SRO or nanoscale precipitates to make dislocation glide more difficult, HEAs may also be designed to delay dislocation nucleation via controlling the HEC in GBs. Consider the five-element HEA shown in Fig. 7a as an example. Via SRO, one/two elements form HECs (Fig. 7c) from the RSS phase (Fig. 7b), while the other elements may form stable LECs/MECs (Fig. 7d). Such an HEA will tend to form a strong matrix largely composed of LECs/MECs, with the less stable HECs primarily located at the GBs. The optimal-sized HECs formed in the GBs (stabilized by surrounding LECs/MECs) can delay dislocation nucleation, thus enhancing strength

(Fig. 7e). Ti is intrinsic HCP element and dynamically unstable in BCC[36]. Therefore, Ti-rich HECs in BCC MoTaTiWZr are favorable for dislocation (HCP structure) nucleation during tension. However, LECs/MECs are W-/Mo-rich, which are intrinsic BCC elements and stable in BCC MoTaTiWZr. Therefore, BCC-stabilized LECs/MECs are not favorable for dislocation nucleation, hence stabilizing the HCP-favorable HECs to prohibit dislocation nucleation. It has also been reported that Ti could be stabilized by Mo[37] and W[40] according to their phase diagram. That is the reason why the LECs/MECs could stabilize HECs.

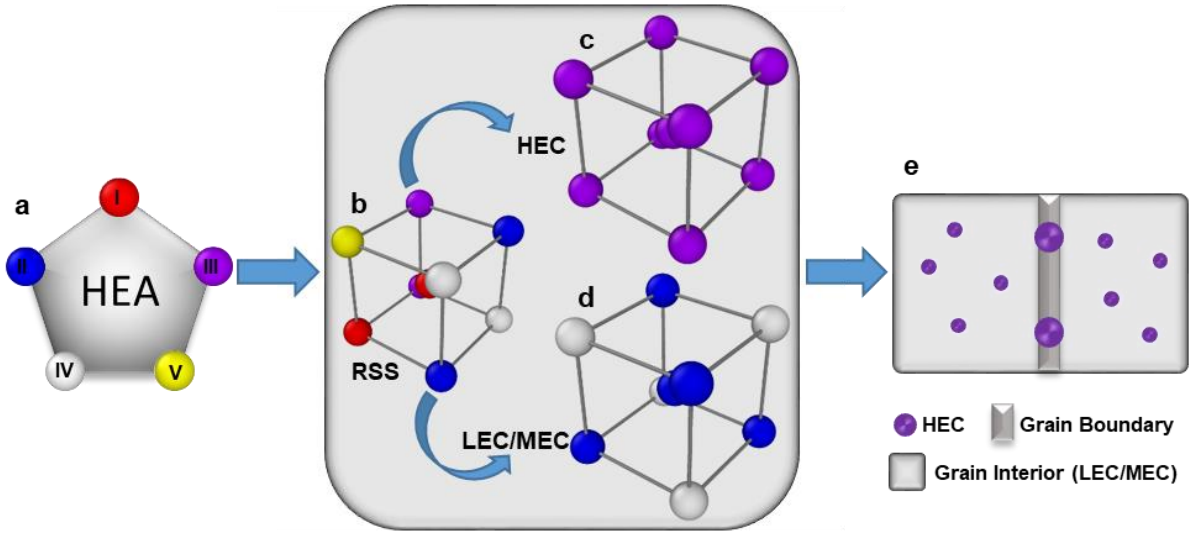

Fig. 7 Schematic diagram illustrating a strategy for designing HEAs with enhanced strength via short-range ordering. a Design a HEA with five elements. Formation of **c** HEC and **d** LEC/MEC via SRO from **b** the RSS. **e** The optimal-sized HECs in grain boundaries (stabilized by surrounding LECs/MECs) delay dislocation nucleation and enhance strength.

Applicability of the design strategy to other RHEAs. A critical component in controlling dislocation nucleation in MoTaTiWZr RHEA is the formation of Ti-rich HECs. We further explore the applicability of our work to other RHEAs by replacing Ti with Nb, Hf, or V. The calculated

cohesive energies of BCC unit cells consisting of Nb-Nb (-7.0 eV), Hf-Hf (-6.6 eV), and V-V (-5.4 eV) using DFT are listed in Supplementary Tables 5a, as compared with that of Ti-Ti (-5.3 eV). Clearly, the energies of Nb-Nb and Hf-Hf are close to those of MECs, while that of V-V is similar to that of Ti-Ti HECs. We further calculate the cohesive energies associated with V in MoTaVWZr (Supplementary Tables 5b) and obtain the chemical affinities of atomic pairs (Supplementary Tables 5c). Interestingly, there also exists a distinct classification of HECs (V-V), MECs (Mo-Zr), and LECs (Ta-W) in MoTaVWZr. Therefore, the conclusions made from MoTaTiWZr should be also applicable to MoTaVWZr. Besides, the HECs, MECs and LECs could also form in non-equiatomic $MoTaV_{0.5}WZr$ or $Mo_{0.5}TaV_{0.5}WZr_{0.5}$. It could be speculated that there are less V-rich HECs in $MoTaV_{0.5}WZr$ and less MoZr-rich MECs in $Mo_{0.5}TaV_{0.5}WZr_{0.5}$, as compared with MoTaVWZr. The formation of more TaW-rich LECs in $MoTaV_{0.5}WZr$ or $Mo_{0.5}TaV_{0.5}WZr_{0.5}$ could be easier to stabilize the HECs to realize the design strategy. Therefore, the design strategy could also be used to design other non-equiatomic alloys. Experimentally observed unexpected dominance of edge dislocations in non-equiatomic $Ti_2ZrHfV_{0.5}Ta_{0.2}$[10] also support this argument.

Conclusions

We perform (1) DFT and MD simulations to examine the accuracy of the interatomic potentials used here for the MoTaTiWZr RHEA, (2) iterative MC and MD simulations to simulate SRO evolution in the RHEA, (3) and then MD simulations to investigate the effect of SRO in GIs and GBs on dislocation activities. The good agreements between our DFT and MD simulations on cohesive energies and between our MD simulations and literature on stacking fault energy and surface energy demonstrate that the interatomic potentials provide reasonable representations of

this RHEA. During SRO formation, Ti-rich HECs (weak) form in both GIs and GBs, Ti-poor LECs (strong) form only within GIs, and MECs form as the matrix. Tensile-deformation simulations indicate that the peak stress of the RHEA is dominated by the dislocation nucleation in the GB Ti-rich HECs. Our results further show that edge dislocations play a comparable (or even dominant) role as compared with screw dislocations in the SRO samples post-yield; this is a unique feature of BCC HEAs as compared with conventional BCC metals/alloys. Hence, SRO can be deployed to increase the energy barriers for edge and screw dislocation motion, making the mobility of edge dislocations comparable to or even lower than screw dislocations. This finding explains the experimentally observed unexpected dominance of edge dislocations in NbTaTiV[8], CrMoNbV[9], $Ti_2ZrHfV_{0.5}Ta_{0.2}$[10], TiZrHfNbTa[11] and MoNbTi[17]. We propose a strategy for enhancing strengths via tuning the HEC sizes in RHEAs. The present study not only reveals the role of SRO in governing dislocation activity in RHEAs, but also provides guidelines for the rational design of HEAs with high-performance mechanical properties for structural material applications.

Methods

Atomic potential. Zhou et al.'s[45] embedded atom model (EAM) potential of MoTaTiWZr was employed to perform hybrid MD and MC simulations using the large-scale atomic/molecular massively-parallel simulator (LAMMPS) package[46]. This atomic potential has been tested in earlier MoTaTiWZr RHEA simulations with reasonable results[47,48]. We further checked the validity of this atomic potential by comparing the cohesive energies of the B2 intermetallic and single-element BCC crystal structures in the MoTaTiWZr RHEA with DFT calculations (Supplementary Table 2). Besides, we also calculated the stacking fault energy and surface energy of RSS MoTaTiWZr RHEA using a simulation model with $5 \times 5 \times 5$ nm^3. A good agreement in

the energetic data was obtained, thus validating the reliability of the atomic potential used in the present study.

Model construction. The lattice constant of the BCC MoTaTiWZr RHEA was set at 3.29 Å (obtained after energy minimization) in a simulation cell containing 108,864 atoms for two equal-sized grains. One grain (G1) was oriented with $[11\bar{2}]$, $[\bar{1}10]$, and $[111]$ directions, and the other grain (G2) was oriented with $[1\bar{1}0]$, $[11\bar{2}]$, and $[111]$ directions aligned, respectively, with *x*, *y* and *z* axes. Both grains were constructed by populating atomic sites randomly with Mo, Ta, Ti, W, and Zr subject to the near-equiatomic elemental composition constraint, *i.e.*, 19.8 atomic percent (at.%) Mo, 20.1 at.% Ta, 19.9 at.% Ti, 20 at.% W, and 22.2 at.% Pd for G1 and 19.6 at.% Mo, 20.4 at.% Ta, 19.9 at.% Ti, 19.6 at.% W, and 20.5 at.% Pd for G2.

Atomic swaps and relaxations. The elemental distribution of the BCC MoTaTiWZr RHEA was optimized by performing MC swaps between atomic pairs at a temperature of 300 K or 1,500 K since the experimental annealing temperature normally is ~ 1,400 K[10] to ~ 1,500 K[8]. The probability of each MC swap was calculated by a transition state theory[49]:

$$P = e^{-\frac{E(i+1)-E(i)}{kT}} \quad (1)$$

where *k* is the Boltzmann constant, and *T* is the temperature. A Metropolis criterion[50] was employed to determine the acceptance of each MC swap by comparing the probability, *P*, with a uniformly-generated random number, $R \in (0, 1)$. If *R* is lower than or equal to *P*, the MC swap is accepted. Otherwise, it is rejected. The MC swaps were iterated with MD relaxations to converge site occupancy and atomic displacements, where 100 MC swaps, followed by up to 100 MD relaxations per iteration, showed good efficiency and were utilized in this study.

Characterization of short-range ordering. Short-range ordering was characterized, using the WCP[32] in the 1st-nearest neighbor shell:

$$WCP_{ij} = 1 - Z_{ij}/(\chi_j Z_i) \quad (2)$$

where Z_{ij} is the number of i-type atoms in the 1st-nearest neighbors of j-type atoms, Z_i is the total number of atoms in the 1st-nearest neighbors of j-type atoms, and χ_i is the atomic fraction of i-type atoms in the RHEA. If $WCP_{ij} < 0$, the ij-type pairs are favourable. Otherwise, the ij-type pairs are randomly distributed if $WCP_{ij} = 0$ or not favourable if $WCP_{ij} > 0$.

Tensile deformation. Uniaxial tensile deformation was employed in the *z*-axis direction with a strain rate of 1×10^8 s^{-1} at 300 K or 1,200 K[8] after being thermally equilibrated in an isothermal-isobaric ensemble (a constant number of particles, pressure, and temperature, *i.e.*, NPT) for 0.2 ns (integration time step: 1 fs). During tensile deformation, the NPT ensemble was applied in the *x*-axis and *y*-axis directions to maintain zero lateral pressure. Periodic boundary conditions were applied in all three directions. Evolution of atomic configurations was analyzed by OVITO[51] via identifying phase structures (CNA) and dislocation characters (DXA). To evaluate the density of dislocation character (%), the angle between the dislocation line direction and burgers vector (Θ) was calculated, and the density ratio of edge-dislocation ($0 \leq \Theta < 30°$ and $150 \leq \Theta < 180°$), screw-dislocation ($60 \leq \Theta < 120°$), and mixed-dislocation ($30 \leq \Theta < 60°$ and $120 \leq \Theta < 150°$) length to the total dislocation length was obtained.

Cohesive energy. Density-functional-theory calculations were performed to determine the cohesive energies of elemental pairs in a B2 structure for binary combinations of {Mo, Ta, Ti, W, Zr, and V} and single elements of {Mo, Ta, Ti, W, Zr, Nb, Hf, and V} in the BCC crystal structure, using the Vienna ab initio simulation package (VASP)[52] with a plane-wave basis and projector

augmented wave (PAW) potentials[53,54]. The Perdew, Burke, and Ernzerhof (PBE) exchange correlation energy functional within the generalized gradient approximation (GGA) was employed[55]. For the B2 structure of a binary alloy, the cohesive energy is:

$$E_{\mathrm{c}}(\mathrm{AB}) = \frac{1}{2}\left[E_{\mathrm{g}}(\mathrm{A}) + E_{\mathrm{g}}(\mathrm{B}) - E_{\mathrm{b}}(\mathrm{AB})\right] \quad (3)$$

where E_{b}(AB) is the energy of the fully-relaxed AB structure, and E_{g}(A) and E_{g}(B) are the energies of isolated A and B atoms in their ground states, respectively. For the single-element structure, the cohesive energy is:

$$E_{\mathrm{c}}(\mathrm{A}) = E_{\mathrm{g}}(\mathrm{A}) - \frac{1}{2}E_{\mathrm{b}}(\mathrm{A}) \quad (4)$$

where E_{b}(A) is the energy of the fully-relaxed BCC structure, and E_{g}(A) is the energy of isolated A atom in the ground state, respectively. The cohesive energies of the B2 intermetallic and single-element BCC crystal structures in the MoTaTiWZr RHEA were also calculated using MD simulations to validate the interatomic potential.

To compute the ground-state energies of the symmetry-broken spin-polarized magnetic ground state of an isolated atom, DFT calculations were performed for a single atom in a large cubic cell ($14 \times 14 \times 14$ Å^3) with periodic boundary conditions to avoid interactions with its periodic images. Relaxation runs were done by performing spin-polarized calculations and by allowing both the ionic positions, cell volume, and cell shape to relax. The convergence tolerance for the electronic self-consistency was set at 10^{-8} eV, and the plane-wave energy cutoff was 800 eV. The energy of the AB structure was calculated by fully-relaxing the ion positions and periodic-cell lattice parameters to attain electronic self-consistency with a tolerance of 10^{-8} eV and a force convergence

tolerance of 10^{-4} eV/Å. A plane-wave energy cutoff of 520 eV and k point mesh of 15 × 15 × 15 per cell were applied for all calculations.

Chemical affinity. Using the cohesive energies determined from the interatomic potential (Supplementary Table 2a), we also calculated normalized cohesive energy values in the RHEAs as,

$$E_n(AB_3) = [E_h - E_c(AB_3)]/[E_h - E_l] \quad (5)$$

$$E_n(A) = [E_h - E_c(A)]/[E_h - E_l] \quad (6)$$

where $E_c(AB_3)$ and $E_c(A)$ are the cohesive energies of an AB_3 B2 and single-element (A) BCC unit cell, E_h and E_l are the highest value and the lowest values of $E_c(AB_3)$ and $E_c(A)$. Using the normalized cohesive energies, we further evaluated the chemical affinity of atomic pairs (Supplementary Table 2c), i.e., high/low cohesive energy indicates weak/strong chemical affinity. We define the chemical affinities (CA) of elemental pairs as[27],

$$CA(AB) = [E_n(AB_3) + E_n(BA_3)]/2 \quad (7)$$

$$CA(AA) = E_n(A) \quad (8)$$

where $E_n(AB_3)$ and $E_n(BA_3)$ are the normalized cohesive energies of AB_3 and BA_3 unit cells, respectively.

Minimum energy-path calculations. To explore the energy barriers of dislocation propagation in the MoTaTiWZr HEA, the energy landscapes of the movements of the 1/2<111>/{110} edge dislocation and 1/2<111> screw dislocation were calculated, using the CINEB method[41]. The length of dislocations is around 15 nm, and the lengths of the other two directions are around 10 nm. The initial configuration is constructed by generating an edge/screw dislocation inside the simulation box and then performing energy minimization at zero stress and zero temperature. The

final configuration is obtained by applying a stress of 500 MPa to the initial configuration at a temperature of 4 K and subsequently performing energy minimization at zero stress and zero temperature. After that, CINEB calculation is carried out to obtain the minimum energy pathways and the corresponding energy barriers at zero temperature using the initial and final configurations without applying external stress. The stropping force tolerance is 0.01 eV/Å. The RMS roughness of dislocations is calculated as:

$$RMS = \sqrt{\frac{1}{n}\sum_{i=1}^{n}\left(d_i - \bar{d}\right)^2} \tag{9}$$

where n is the number of atoms forming the dislocation, d_i is the coordinate of the atom, i, along the motion direction of the dislocation, and $\bar{d}$ is the average value of all the d_i.

Acknowledgements

The contributions of S. C. in this paper were sponsored by Shanghai Pujiang Program (Grant No. 22PJ1403700). S. C., Z. H. A., Z. G. Y., and Y.-W. Z. gratefully acknowledge the financial support from the Agency for Science, Technology and Research (A*STAR) under grant AMDM A1898b0043, and the use of computing resources at the A*STAR Computational Resource Centre and National Supercomputer Centre, Singapore. P. K. L. gratefully acknowledges the support of (1) the National Science Foundation (DMR-1611180 and 1809640) with program directors, Drs. J. Yang, G. Shiflet, and D. Farkas and (2) the US Army Research Office (W911NF-13–1-0438 and W911NF-19–2-0049) with program managers, Drs. M. P. Bakas, S. N. Mathaudhu, and D. M. Stepp. The contributions of D. J. S. and S. P. in this paper were fully supported by a grant from the Research Grants Council of the Hong Kong Special Administrative Region, China (Project No. 11211019).

Author contributions

Shuai Chen: Investigation, Conceptualization, Methodology, Software, Data curation, Formal analysis, Validation, Visualization, Writing - original draft, Writing - review & editing. **Zachary H. Aitken**: Software, Formal analysis, Writing - review & editing. **Subrahmanyam Pattamatta**: Methodology, Software, Data curation**. Zhaoxuan Wu**: Methodology, Software, Formal analysis. **Zhigen Yu**: Resources, Software, Validation, Formal analysis. **David J. Srolovitz**: Formal analysis, Writing - review & editing, Funding acquisition, Supervision. **Peter K. Liaw**: Investigation, Formal analysis, Writing - review & editing, Funding acquisition. **Yong-Wei Zhang**: Conceptualization, Formal analysis, Writing - review & editing, Funding acquisition, Project administration, Supervision.

Competing interests

The authors declare no competing interests.

Supplementary data

Supplementary data to this article can be found online.

Data availability

The raw/processed data required to reproduce these findings cannot be shared at this time as the data also forms part of an ongoing study.

References

[1] Cantor, B., Chang, I. T. H., Knight, P. & Vincent, A. J. B. Microstructural development in equiatomic multicomponent alloys. *Mater. Sci. Eng. A* **375**, 213–218 (2004).

[2] Yeh, J.-W. et al. Nanostructured high-entropy alloys with multiple principal elements: novel alloy design concepts and outcomes. *Adv. Eng. Mater.* **6**, 299–303 (2004).

[3] George, E. P., Raabe, D. & Ritchie, R. O. High-entropy alloys. *Nat. Rev. Mater.* **4** 515–534 (2019).

[4] Yang, T. et al. Ultrahigh-strength and ductile superlattice alloys with nanoscale disordered interfaces. *Science* **369**, 427–432 (2020).

[5] Shi, P. et al. Hierarchical crack buffering triples ductility in eutectic herringbone high-entropy alloys. *Science* **373**, 912–918 (2021).

[6] Chen, S. et al. Real-time observations of TRIP-induced ultrahigh strain hardening in a dual-phase CrMnFeCoNi high-entropy alloy. *Nat. Commun.* **11**, 826 (2020).

[7] Shi, P. et al. Enhanced strength-ductility synergy in ultrafine-grained eutectic high-entropy alloys by inheriting microstructural lamellae. *Nat. Commun.* **10**, 489 (2019).

[8] Lee, C. et al. Temperature dependence of elastic and plastic deformation behavior of a refractory high-entropy alloy. *Sci. Adv.* **6**, eaaz4748 (2020).

[9] Lee, C. et al. Strength can be controlled by edge dislocations in refractory high-entropy alloys. *Nat. Commun.* **12**, 5474 (2021).

[10] Li, T., Lu, Y., Li, Z., Wang, T., Li, T. Hot deformation behavior and microstructure evolution of non-equimolar $Ti_2ZrHfV_{0.5}Ta_{0.2}$ refractory high-entropy alloy. *Intermetallics* **146**, 107586 (2022).

[11] Dirras, G. et al. Microstructural investigation of plastically deformed $Ti_{20}Zr_{20}Hf_{20}Nb_{20}Ta_{20}$ high entropy alloy by X-ray diffraction and transmission electron microscopy. *Mater. Charact.* **108**, 1 (2015).

[12] Ma, E. Unusual dislocation behavior in high-entropy alloys. *Scr. Mater.* **181**, 127–133 (2020).

[13] Chen, B., Li, S., Zong, H., Ding, X., Sun, J. & Ma, E. Unusual activated processes controlling dislocation motion in body-centered-cubic high-entropy alloys. *Proc. Natl. Acad. Sci. U.S.A.* 117, 16199–16206 (2020).

[14] Zhang, Y. et al. Microstructures and properties of high-entropy alloys. *Prog. Mater. Sci.* **61**, 1–93 (2014).

[15] Caillard, D. Kinetics of dislocations in pure Fe. Part I. In situ straining experiments at room temperature. *Acta Mater.* **58**, 3493–3503 (2010).

[16] Yin, S. et al. Atomistic simulations of dislocation mobility in refractory high-entropy alloys and the effect of chemical short-range order. *Nat. Commun.* **12**, 4873 (2021).

[17] Wang, F. et al. Multiplicity of dislocation pathways in a refractory multiprincipal element alloy. *Science* **370**, 95–101 (2020).

[18] Varvenne, C., Luque, A. & Curtin, W. A. Theory of strengthening in FCC high entropy alloys. *Acta Mater.* **118**, 164–176 (2016).

[19] Maresca, F. & Curtin, W. A. Mechanistic origin of high strength in refractory BCC high entropy alloys up to 1900K. *Acta Mater.* **182**, 235–249 (2020).

[20] Yin, B., Maresca, F., Curtin, W. A. Vanadium is an optimal element for strengthening in both fcc and bcc high-entropy alloys. *Acta Mater.* **188**, 486–491 (2020).

[21] Tong, Y., Zhao, S., Bei, H., Egami, T., Zhang, Y. & Zhang, F. Severe local lattice distortion in Zr- and/or Hf-containing refractory multi-principal element alloys. *Acta Mater.* **183**, 172–181 (2020).

[22] Ding, Q. et al. Tuning element distribution, structure and properties by composition in high-entropy alloys. *Nature* **574**, 223–227 (2019).

[23] Zhang, R. et al. Short-range order and its impact on the CrCoNi medium-entropy alloy. *Nature* **581**, 283–287 (2020).

[24] Chen, X. et al. Direct observation of chemical short-range order in a medium-entropy alloy. *Nature* **592**, 712–716 (2021).

[25] Ma, E. & Wu, X. Tailoring heterogeneities in high-entropy alloys to promote strength-ductility synergy. *Nat. Commun.* **10**, 5623 (2019).

[26] Chen, S. et al. Simultaneously enhancing the ultimate strength and ductility of high-entropy alloys via short-range ordering. *Nat. Commun.* **12**, 4953 (2021).

[27] Chen, S. et al. Chemical-affinity disparity and exclusivity drive atomic segregation, short-range ordering, and cluster formation in high-entropy alloys. *Acta Mater.* **206**, 116638 (2021**)**.

[28] Zunger, A., Wei, S.-H., Ferreira, L. G. & Bernard, J. E. Special quasirandom structures. *Phys. Rev. Lett.* **65**, 353–356 (1990).

[29] Jiang, C. & Uberuaga, B. P. Efficient ab initio modeling of random multicomponent alloys. *Phys. Rev. Lett.* **116**, 105501 (2016).

[30] Sorkin, V., Chen, S., Tan, T. L., Yu, Z. G., Man, M. & Zhang, Y.-W. First-principles-based high-throughput computation for high entropy alloys with short range order. *J. Alloys Compd.* **882**, 160776 (2021).

[31] Li, X.-G., Chen, C., Zheng, H., Zuo, Y. & Ong, S. P. Complex strengthening mechanisms in the NbMoTaW multiprincipal element alloy. *npj Comput. Mater.* **6**, 70 (2020).

[32] Cowley, J. M. X-ray measurement of order in single crystals of Cu_3Au. *J. Appl. Phys.* **21**, 24–30 (1950).

[33] Hu, Y.-J., Sundar, A., Ogata, S., Qi, L. Screening of generalized stacking fault energies, surface energies and intrinsic ductile potency of refractory multicomponent alloys. *Acta Mater.* **210**, 116800 (2021).

[34] Faken, D. & Jónsson, H. Systematic analysis of local atomic structure combined with 3D computer graphics. *Comput. Mater. Sci.* **2**, 279–286 (1994).

[35] Stukowski, A., Bulatov, V. V. & Arsenlis, A. Automated identification and indexing of dislocations in crystal interfaces. *Modelling Simul. Mater. Sci. Eng.* **20**, 085007 (2012).

[36] Mei, Z.-G., Shang, S.-L., Wang, Y. & Liu, Z.-K. Density-functional study of the thermodynamic properties and the pressure-temperature phase diagram of Ti. *Phys. Rev. B* **80**, 104116 (2009).

[37] Shim, J.-H., Oh, C.-S. & Lee, D. N. A thermodynamic evaluation of the Ti-Mo-C system. *Metall. Mater. Trans. B* **27B**, 955 (1996).

[38] Barzilai, S., Toher, C., Curtarolo, S. & Levy, O. Evaluation of the tantalum-titanium phase diagram from ab-initio calculations. *Acta Mater.* **120**, 255–263 (2016).

[39] Chinnappan, R., Panigrahi, B. K. & Walle, A. van de. First-principles study of phase equilibrium in Ti–V, Ti–Nb, and Ti–Ta alloys. *CALPHAD* **54**, 125 (2016).

[40] Ångqvist, M., Rahm, J. M., Gharaee, L. & Erhart, P. Structurally driven asymmetric miscibility in the phase diagram of W-Ti. *Phys. Rev. Mater.* **3**, 073605 (2019).

[41] Henkelman, G., Uberuaga, B. P., & Jónsson, H. A climbing image nudged elastic band method for finding saddle points and minimum energy paths. *J. Chem. Phys.* **113**, 9901–9904 (2000).

[42] Li, L. et al. Segregation-driven grain boundary spinodal decomposition as a pathway for phase nucleation in a high-entropy alloy. *Acta Mater.* **178**, 1–9 (2019).

[43] Liu, L. et al. Nanoprecipitate-strengthened high-entropy alloys. *Adv. Sci.* **8**, 2100870 (2021).

[44] Wei, S. et al. Natural-mixing guided design of refractory high-entropy alloys with as-cast tensile ductility. *Nat. Mater.* **19**, 1175–1181 (2020).

[45] Zhou, X. W. et al. Misfit-energy-increasing dislocations in vapor-deposited CoFe/NiFe multilayers. *Phys. Rev. B* **69**, 144113 (2004).

[46] Plimpton, S. Fast parallel algorithms for short-range molecular dynamics. *J. Comput. Phys.* **117**, 1–19 (1995).

[47] Singh, P. et al. Design of high-strength refractory complex solid-solution alloys. *npj Comput. Mater.* **4**, 16 (2018).

[48] Sharma, A. et al. Pseudoelastic deformation in Mo-based refractory multi-principal element alloys. *Acta Mater.* **220**, 117299 (2021).

[49] Nitzan, A. Chemical dynamics in condensed phases: relaxation, transfer and reactions in condensed molecular systems. Oxford university press (2006).

[50] Metropolis, N., Rosenbluth, A. W., Rosenbluth, M. N., Teller, A. H. & Teller, E. Equation of state calculations by fast computing machines. *J. Chem. Phys.* **21**, 1087–1092 (1953).

[51] Stukowski, A. Visualization and analysis of atomistic simulation data with OVITO-the open visualization tool. *Model. Simulat. Mater. Sci. Eng.* **18**, 15012 (2009).

[52] Kresse, G. & Furthmüller, J. Efficient iterative schemes for ab initio total-energy calculations using a plane-wave basis set. *Phys. Rev. B* **54**, 11169–11186 (1996).

[53] Blöchl, P. E. Projector augmented-wave method. *Phys. Rev. B* **50**, 17953–17979 (1994).

[54] Kresse, G. & Joubert, D. From ultrasoft pseudopotentials to the projector augmented-wave method. *Phys. Rev. B* **59**, 1758–1775 (1999).

[55] Perdew, J. P., Burke, K., & Ernzerhof, M. Generalized gradient approximation made simple. *Phys. Rev. Lett.* **77**, 3865–3868 (1996).